Energy & Environmental Science

ROYAL SOCIETY OF CHEMISTRY

PAPER

View Article Online
View Journal

Cite this: DOI: 10.1039/d6ee01258b

The critical role of water structure in anion transport

Keenan Smith,[a] Arun Prakash Periasamy,[b] Quentin Berrod,[c] Jean-Marc Zanotti,[d] Markus Appel,[e] Victoria Garcia Sakai,[f] Andrew Seel,[fg] Thomas F. Headen,[f] Bettina Schwaighofer,[e] Daniel J. L. Brett,[h] Thomas S. Miller,[i] Christian D. Lorenz,[j] John R. Varcoe,[b] Sandrine Lyonnard *[c] and Fabrizia Foglia *[a]

Received 25th February 2026,
Accepted 16th June 2026

DOI: 10.1039/d6ee01258b

rsc.li/ees

The molecular mechanisms that couple ion motion, water dynamics, and polymer relaxation remain elusive. However, they are critical for applications such as fuel cells and electrolysers where ion and water transport through anion-exchange membranes (AEMs) govern the performance. Here, multi-resolution neutron spectroscopy measurements are combined with molecular simulations to directly resolve ion-specific transport processes in a radiation-grafted polyethylene-based AEM. By capturing molecular motions over picosecond-to-nanosecond timescales, we reveal dynamic coupling between polymer segmental motion and nanoconfined water species, as well as strikingly distinct hydration structures around OH^- and Cl^- ions. Water is shown to orchestrate ion mobility by forming ion-dependent hydrogen-bond networks that evolve with composition, temperature, and humidity, ultimately dictating conductivity. These insights establish water not merely as a passive medium but as an active structural and transport agent. This molecular-level understanding provides a framework for the rational design of next-generation AEMs with enhanced efficiency, stability, and sustainability for electrochemical energy conversion.

Broader context

The transition to a carbon-neutral society depends critically on transformative advances in ion-conducting materials that underpin electrochemical energy technologies such as fuel cells and electrolysers. Efficient ion transport within functional membranes is central to their performance, yet optimising these systems requires a fundamental understanding of the structure–transport relationship that governs ionic mobility under operating conditions. While ion transport in dilute aqueous solution is well understood, transport within soft, nanoconfined, hydrogen-bonded environments remain a major scientific challenge. In these complex media, collective molecular dynamics, rather than single-particle diffusion alone, govern macroscopic charge transport. Here, by integrating multi-resolution neutron spectroscopy with molecular simulations, we directly resolve how ion organisation couples to water networks and polymer relaxations to control charge transport. We demonstrate that hydroxide and chloride ions induce fundamentally distinct hydration topologies and dynamic correlation lengths within confined polymer environments. These differences redefine ionic conductivity under confinement as an emergent property of collective ion–water–polymer dynamics, rather than an intrinsic property determined solely by individual ion diffusivity. Together, these insights establish a mechanistic framework for the predictive, physics-based design of next-generation ion-conducting materials.

[a] Department of Chemistry, Christopher Ingold Laboratory, University College London, 20 Gordon St., London, WC1H 0AJ, UK. E-mail: f.foglia@ucl.ac.uk
[b] School of Chemistry and Chemical Engineering, University of Surrey, Guildford, Surrey, GU2 7XH, UK
[c] Université Grenoble Alpes, CNRS, CEA, Grenoble INP, IRIG, SyMMES, 38000, Grenoble, France. E-mail: sandrine.lyonnard@cea.fr
[d] Laboratoire Léon Brillouin (CEA–CNRS), Université Paris-Saclay, CEA Saclay, 91191 Gif-sur-Yvette Cedex, France
[e] Institut Laue Langevin, 71 avenue des Martyrs, CS 20156, 38042, Grenoble CEDEX 9, France
[f] ISIS Neutron and Muon Source, Rutherford Appleton Laboratory, Harwell Science and Innovation Campus, Chilton, OX11 0QX, UK
[g] Department of Physics, Royal Holloway University of London, Egham Hill, Egham, TW20 0EX, UK
[h] Prosemino Limited, Paper Yard Quebec Way, London, SE16 7LG, UK
[i] Electrochemical Innovation Lab, Department of Chemical Engineering, University College London, Torrington Place, London, WC1E 7JE, UK
[j] Department of Engineering, King's College London, Strand Campus, London, WC2R 2LS, UK

Background and context

Ion size and charge density critically influence the local structure and dynamics of water. In bulk solutions, small, highly charged ions such as Li^+ strongly interact with surrounding water molecules, forming tightly bound hydration shells that disrupt the hydrogen-bond network.[1,2] In contrast, larger ions with lower charge densities, such as Cl^-, interact more weakly, producing diffuse hydration structures and less perturbation of water–water hydrogen bonding.[1,2] These ion-specific effects modulate water reorientation and diffusion dynamics, ultimately impacting ion mobility and conductivity. In aqueous LiCl solutions, dynamic crossovers and multiple relaxation modes are associated with water motion, highlighting the influence of ionic character on hydrogen-bond rearrangements.[3,4] Analogous mechanisms govern proton transfer in hydrogen-bonded networks where first-principles simulations show that protons can propagate along transient "water wires" spanning several hydrogen bonds, emphasising the critical role of water structure in charge transport.[5] Coordinated H-bond rearrangements in the second hydration shell favour fast H^+ and OH^- charge transfer events, *e.g. via* the so-called "structural diffusion" which is the dominant mechanism in highly hydrated systems.[6–9]

Ion-specific effects are also of paramount importance in polymeric environments such as proton exchange membranes (PEM) or anionic exchange membranes (AEM) where ion-selective conducting properties[10,11] are targeted for a wide range of applications and devices.[12–16] The significant influence ions can exert on water structure and dynamics is recognised to play a key role in the overall efficiency of these systems,[10,11,17] but a detailed microscopic description of ion–water–polymer interactions is lacking.[17,18] It is critical to rationalise how the nature and size of the ion can influence its ability to interact with the polymer matrix. Small ions may disrupt polymer chain conformations and create additional pathways for water and ion movement, but they may also coordinate with polymer moieties, inducing local cross-links that require activated chain dynamics to be overcome.[19] Unlocking the full potential of ionic membranes demands rigorous and integrated consideration of these coupled factors, necessitating dedicated studies that explicitly resolve ion-specific interactions, polymer chemistry, and water-mediated transport mechanisms.

Several AEM candidates are being designed to enable stable OH^- transport in fuel cells and water electrolyser cells for green hydrogen applications. A key challenge in these technologies is to enable sufficient ion transport at low hydration, requiring tailoring of properties *via* chemical design.[20,21] Beyond conventional candidates such as poly(aryl piperidinium)- and poly(phenylene oxide)-based AEMs,[22] high-density polyethylene (HDPE)-based AEMs[23] are being actively studied for their robustness, high ion conductivity, and facile water transport properties.[24,25] Water management is not merely operational, it is performance-defining. Enhanced water transport suppresses excessive hydration that can cause cathode flooding while simultaneously enabling higher current densities. Because water interacts intimately with both the polymer backbone and the mobile ions, membrane performance is intrinsically governed by the interplay between hydration networks and polymer microstructure. In radiation-grafted (RG) systems, parameters such as crystallite size, distribution, and spatial organisation directly influence transport pathways and electrochemical behaviour.[23,26–28] Understanding and controlling this structure–hydration–transport coupling is therefore essential for translating promising materials into high-performance, durable electrochemical devices.

Despite its importance, the microscopic details of water-mediated conduction mechanism in this system remain unknown. Existing studies provide only partial insight, typically confined to limited ion chemistries and narrow hydration regimes.[17] Therefore, until a deeper understanding of how water-enabled ion transport is achieved, membrane and device optimisation will remain largely empirical.

To address this gap, we designed a study where we use Cl^- and OH^- forms of the HDPE-based RG_AEM (Fig. 1a) to specifically tackle the ion–water–polymer coupling. HDPE provides an ideal platform: it is a well-characterised, mechanically robust system with demonstrated relevance for fuel cells and electrolysers, yet it exhibits pronounced ion-specific conductivity differences, particularly under low-hydration conditions. This combination of structural simplicity, technological relevance, and strong ion-dependent transport makes it uniquely suited for a multi-scale experimental-theoretical investigation.

Strikingly, comparison of the Cl^- and OH^- form reveals remarkable anionic conductivities at unexpectedly low hydration levels at 323 K (Fig. 1b and c). The OH^- form exhibits conductivity 4.5-fold higher than in the Cl^- form at high hydration ($\lambda = n[H_2O]/[TMA^+] = 13$; TMA is trimethylammonium) and nearly 20-fold higher at low hydration regime ($\lambda = 4$). These differences cannot simply be ascribed to the intrinsic diffusivities of ions at infinite dilutions (5.27 *vs.* 2.03×10^{-5} $cm^2\ s^{-1}$; for OH^- and Cl^-, respectively[30,31]). Therefore, a distinct mechanism for the transport of OH^- and Cl^- ions must occur in the hydrated membrane, suggesting distinct underlying links between ion motions and water dynamics.

To resolve these mechanisms, we present a multi-technique characterisation combining chemical analysis, neutron scattering and molecular simulations to understand how the presence of OH^- and Cl^- alters the structure and dynamics of water molecules within HDPE-based membranes, and how these alterations impact overall membrane performance. A series of membranes was prepared at different hydration levels (λ = 2, 4, and 13; supplementary information (SI) Text S1).

Multi-resolution Quasi-Elastic Neutron Scattering (QENS) was performed to access motions in the ps–ns timescale (Fig. 1e). In this range, fast molecular rotations of specific chemical groups, ionic mobility and polymer relaxations can be isolated and followed as a function of hydration and ionic composition. To carefully examine the impact of ions on the water properties, the HDPE-based RG_AEM samples were studied in various states: (i) OH^- membrane hydrated in either H_2O or D_2O (designated OH^-/H_2O and OD^-/D_2O, respectively); (ii) Cl^- membrane hydrated in either H_2O or D_2O (designated Cl^-/H_2O and Cl^-/D_2O, respectively); and (iii) "formally dry" samples studied under anhydrous conditions (*e.g.*, $\lambda = 2$ in the OH^- form). Note that different solvent

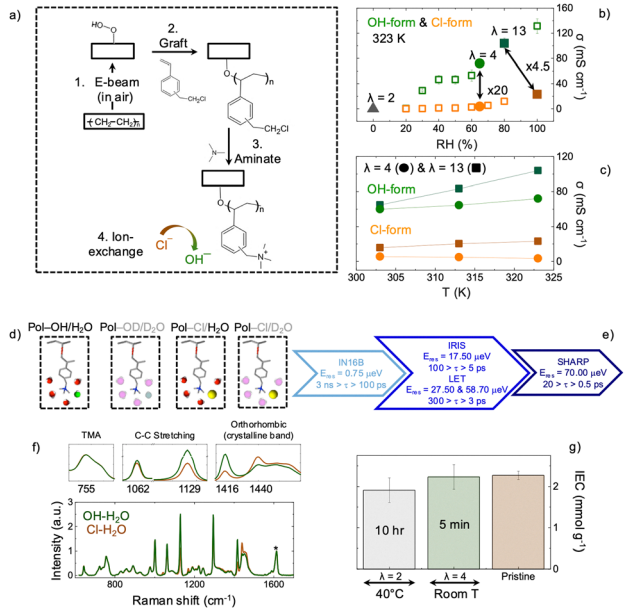

Fig. 1 (a) An outline of the radiation-grafted anion-exchange membranes (RG-AEM) used in this study, made from high-density polyethylene (HDPE). (b) and (c) Ionic conductivity as a function of relative humidity and temperature, respectively, for OH^- and Cl^- forms (represented by orange and green symbols; respectively). The measurements were performed under controlled temperature (*e.g.*, 323 K; panel b) and humidity (λ = 2, 4, 13; black triangle, circle and solid square symbols; respectively) conditions to evaluate the effect of ion exchange and environmental parameters on membrane transport performance. OH^- conductivity tests were carried out using Dekel's method,[29] which prevents the formation of HCO_3^-. (d) Chemically and isotopically substituted AEM used to investigate different aspects of the dynamics. In the label, the neutron-visible and -invisible species are reported in black and in grey; respectively. (e) Timescales probed using neutron spectroscopy at instruments with different energy resolution characteristics. (f) Raman spectra collected on HDPE-TMA-RG_AEM in its Cl^- form (brown spectrum, where the sample had not been exposed to any high pH or low hydration conditions) and on the samples after re-conversion back to the Cl^- form after OH^- form handling (green spectrum). The spectra were normalised to the intensity of the 1612 cm^{-1} band (aromatic ring quadrant mode in the grafted poly(VBC) chains). (g) Ion-exchange capacities (IEC) for Cl^- form HDPE-TMA-RG_AEM samples after they had been treated to different hydration states in the OH^- forms (grey and green bars; dehydrated at 40 °C [λ = 2] and room temperature [λ = 4]; respectively) compared to its pristine Cl^- [non-alkali-treated] form (brown bar).

deuteration (H_2O and D_2O; Fig. 1d) was used to take advantage of the large difference in neutron scattering cross-section between H and D isotopes, which enables isolation of the dynamics of individual components in the complex ion–water–polymer system. The D_2O-hydrated samples define the baseline associated with polymer dynamics under the various hydration conditions.

The systematic comparison of all these samples allowed the separation of contributions from the polymer backbone, solvent, and ions, thereby clarifying how ionic species influence water properties in hydrated membranes. Additionally, total scattering measurements and classical molecular dynamics (MD) simulations were performed to characterise the H-bond network in both the OH^- and Cl^- forms. Altogether the results allow us to develop a detailed understanding of the remarkable anionic conductivity observed for both the OH^- and Cl^- form of HDPE RG_AEMs at unexpectedly low hydration levels. They also unravel the number and type of water molecules involved in the ion-specific, hydration-dependent transfer mechanism.

Experimental procedures

Sample preparation

The benzyltrimethylamonium-type HDPE-based radiation-grafted anion-exchange membranes were synthesised as previously reported (with a pristine as-synthesised Cl^-; IEC = 2.3 mmol g^{-1} and a fully hydrated thickness of 25–30 μm).[32] Activated polyethylene films generated by electron-beam treatment act as radical initiators for the grafting of vinyl monomers such as vinylbenzyl chloride (VBC), producing polymer chains distributed throughout the membrane bulk. Subsequent amination yields radiation-grafted AEMs bearing covalently bound cationic sites (*e.g.*, quaternary ammonium, QA) balanced by mobile anions such as OH^-, Cl^- (or HCO_3^-/CO_3^{2-}) depending on the target electrochemical application.[23]

Samples were tested in three ionic and isotopic forms: (i) Cl^-/D_2O (to minimise the signal form water and ion, to best study the polymer); (ii) Cl^-/H_2O (to directly compare the QENS and conductivity results); and (iii) in OH^- form (to enhance the signal from OH). For scattering experiments, the OH^- form was produced by immersing in 1 M NaOH at room temperature for 1 h under inert atmosphere, changing the solution three times to ensure the complete ion exchange. Membranes were washed in pure water to remove any excess of NaOH; water resistance confirmed the effective removal. Experiments were carried out at water contents ranging between high (λ = 13) to formally dry (λ = 2) hydration levels, expressed as the number of water molecules per functional group ($\lambda = (M_{H_2O}/Mw_{H_2O})/(IEC w_{dry})$). Hydration levels were obtained by removing the excess of water by drying the membrane in a vacuum oven at room temperature.

QENS experiments

Four neutron spectrometers were used: (1) SHARP[33] (run by LLB – Léon Brillouin Laboratory – and located at ILL, France), to investigate relaxation dynamics on a picosecond timescale; (2) LET[34] & IRIS[34] (ISIS, UK), to study dynamics on the ten to hundred picosecond timescale; and (4) IN16B[33] (ILL, France) to probe nanosecond timescales. TOF experiments were performed using an incident wavelength of 5.12 Å (E_{res} = 70.0 μeV; SHARP); this configuration allows probing motions in the picosecond timescale of $0.5 < \tau < 20$ ps. Dynamics in the range $5 < \tau < 100$ ps were probed using either LET experiments which were performed using an incident energy of either 1.8 or 3.2 meV (E_{res} = 27.5 and 58.7 μeV, respectively), or IRIS experiments acquired using the PG002 analyser crystal set-up (E_{res} = 17.5 μeV). Motions in the nanosecond timescale ($0.1 < \tau < 3$ ns) were performed on IN16B using an incident wavelength of 6.271 Å (E_{res} = 0.75 μeV). The combination of these instruments allows coverage of the extended timescale range typically needed in hydrated membranes to access fast molecular rotations (usually sub-ps), jump diffusive motions (usually from ps to 100 ps) and slow ionic hopping events or slow polymer relaxations (longer than 100 ps).

Elastic fixed window scan (EFWS) data were recorded while heating (SHARP and IN16B) or cooling (IRIS) the sample; inelastic fixed window scan (IFWS) data were recorded either by adjusting the Doppler speed on IN16B to achieve $\Delta E = 3$ μeV energy offsets.[35] AEM samples were wrapped in aluminium foil and then loaded into either flat (4 cm × 5 cm) or annular aluminium cells sealed with indium.

Vanadium reference and empty can measurements were performed for data normalisation. Scattering profiles were acquired in T-range from 230 to 330 K, in different ionic (Cl^- *vs.* OH^-) and isotopic forms (H_2O- and D_2O-hydrated), as well as hydration levels (λ = 2, 4, and 13).

Different contributions to the relaxation dynamics operating at different timescales can be found in QENS data and are treated with multi-Lorentzian components where their width and intensity provide information on the dynamics (*e.g.*, local *vs.* diffusive motions). Initially, the theoretical $S(Q,\omega)$ and instrumental resolution ($R(\omega)$) are convoluted to evaluate the experimental $S(Q,\omega)$ datasets. This entails building a model that includes all the different dynamics that can overlap. Hence, the scattering data are analysed using a single analytical correlation function, in which the weights assigned to the various components are determined by the analysis window. Protons moving faster than the spectroscopic window will, in general, be integrated into an almost flat background (*i.e.*, a Lorentzian function with a width such that it appears almost flat in the investigated energy-transfer scale), while protons moving slower than the spectroscopic window will be integrated into the elastic component (instrument-dependent and evaluated by the scattering profile acquired at 2 K).

Total scattering experiments

Data were collected using the NIMROD[34,36] instrument at the ISIS Spallation Neutron and Muon Source (ISIS, UK). Weighed samples in either Cl^- or OH^- form hydrated in H_2O to the $\lambda = 4$ form were sealed inside a flat-geometry, null-scattering TiZr alloy cell and measured on the order of 6 hours, for integrated currents of 240 μA. After measurements, the samples were removed from the cell, dried, and rehydrated to the same λ = 4 form in D_2O. The mass of membrane and hydration level were therefore kept consistent between measurements, with only the H_2O/D_2O content differing between samples of the same Cl^- or OH^- form.

A total scattering measurement on NIMROD measures the total structure factor, which for a system of n different chemical species is expressed by:

$$F(Q) = \sum_{\alpha=1}^{n}\sum_{\beta=1}^{n} c_\alpha c_\beta b_\alpha b_\beta \left[S_{\alpha\beta}(Q) - 1\right] \quad (1)$$

where b_α is the bound coherent neutron scattering length of species α with atom-fraction c_α. $S_{\alpha\beta}(Q)$ is the Faber-Ziman partial structure factor for species α, β.

By taking measurements for the same membrane in H_2O and D_2O form, the difference between the measured total structure factors removes all membrane–membrane partial structure factors, or any partial structure factors not including the water protons/deuterons. As such:

$$\Delta F(Q) = F(Q)_D - F(Q)_H = c_H{}^2\left(b_D{}^2 - b_H{}^2\right)\left[S_{HH}(Q) - 1\right] + \sum_X 2c_H c_X (d_D - b_H) b_X \left[S_{XH}(Q) - 1\right] \quad (2)$$

where we denote the sum over X being all $S_{HX}(Q)$ partials where X is any species other than the water proton (including membrane protons). $\Delta F(Q)$ represents a water proton-centred partial structure factor for the water molecules within the water–membrane system.

Prior to subtraction, data were treated in the Gudrun package,[37,38] using standardised routines for the removal of sample-dependant incoherence and inelasticity corrections.

IEC measurements

The dry mass (m_d; g) of each vacuum-dried (50 °C for 4 h) HDPE-TMA-RG_AEM sample (either in as-synthesised pristine Cl^- form and after being ion-exchanged back to the Cl^- form after OH^- form evaluation) was recorded using a METLER TOLEDO analytical balance (Model MS204S, Switzerland). Each vacuum-dried sample was then immersed in aqueous $NaNO_3$ (20 cm^3, 2.4 mol dm^{-3}, significant excess of $NO_3{}^-$ anions) and stirred overnight to release the Cl^- ions from the AEM sample. Aqueous HNO_3 (1 cm^3, 2 mol dm^{-3}) was then added into the $NaNO_3$ solutions (still containing the HDPE-RG_AEM sample) and titrated with $AgNO_3$ (20.00 ± 0.06 mmol dm^{-3}) using the Metrohm 848 Titirino plus auto titrator equipped with Ag–Titrode. The endpoint (EP; cm^3) was taken as the steepest gradient on the potential *vs.* volume curve. The IEC of each sample (mmol g^{-1}) was calculated from the EP, the dry mass, and the standardised $AgNO_3$ concentration received, using: IEC = (EP × 0.02M)/m_d. The IEC of each sample was recorded as an average from individual titrations on n = 3 repeat samples (reported errors are sample standard deviations).

$NaNO_3$ solid, analytical grade standardised aqueous $AgNO_3$ (20.00 ± 0.06 mmol dm^{-3}), and aqueous HNO_3 (2.0 mol dm^{-3}) were used as received from Fisher Scientific. Analytical grade aqueous NaCl (1.0 mol dm^{-3}) and KOH (1.0 mol dm^{-3}) were used as received from Merck.

Conductivity studies

In-plane OH^- and Cl^- conductivity of HDPE-RG_AEM samples (2.5 cm ×1 cm) were determined using the method proposed by Dekel to ensure removal of carbonates.[29] AC electrochemical impedance spectroscopy (EIS) using a frequency response analyser (Gamry, UK) with an oscillating voltage of 10 mV over a frequency range of 1 MHz–1 Hz was employed in combination with a BekkTech four-point probe conductivity cell. Four equally spaced Pt electrodes, held in contact with the membrane. The ion conductivity (σ; S cm^{-1}) of the membrane was obtained according to; $\sigma = l/RWt$, where l = 0.425 cm is the fixed distance between the two inner Pt electrodes; R is the membrane resistance (Ω) corresponding to the high frequency X-intercept of the real axis in the Nyquist plot; W is the membrane width (cm) and t is the membrane thickness (cm). Humidity and temperature in

the BekkTech cell were maintained by use of a Scribner Associates 850e test rig (Scribner, USA) with flowing N_2 (0.5 L min^{-1}) gas at controlled temperature. The membrane was allowed to equilibrate for at least 2 hours at each temperature and RH condition prior to measurement.

Raman analysis

The Raman spectrum of each HDPE-RG_AEM sample (either in as-synthesised pristine Cl^- form and after being ion-exchanged back to the Cl^- form after OH^- form evaluation) was collected at 10 random spots using an InVia Reflex Raman Microscope (Renishaw, UK). Each spectrum was recorded using 785 nm excitation (near IR line laser, 100% laser power, pin in), a 20× objective lens (NA = 0.40) and 1 s exposure times per spectra. The 10 spectra from each sample were baseline corrected, normalised to the intensity of HDPE-derived 1295 cm^{-1} band and averaged using Spectragryph to produce a single spectrum per sample.

Simulation studies

Simulations were conducted on four different ionic solutions, as shown in Table S2. In each system, the interactions between the ions and water were modelled using the CHARMM36 forcefield.[39] The initial systems and the files required for the simulations were generated using CHARMM-GUI.[40,41] A similar simulation protocol was used for each system. First, an energy minimisation of the system was performed using the steepest descent algorithm. Then a simulation using the NVT ensemble with the Nose–Hoover thermostat to keep the temperature around 300 K was performed with a 1 fs timestep and was run for 125 ps. Next, a simulation using the NPT ensemble with the same thermostat and an isotropic Parrinello–Rahman barostat to maintain a temperature of 300 K and a pressure of 1 bar. This simulation used a 1 fs timestep and ran for 500 ps. Finally, a production simulation was conducted using the NPT ensemble with the same thermostat and barostat. This simulation was run for 200 ns with a 2 fs timestep. In all these simulations, a cut-off of 1.2 nm was used for the LJ interactions and for the explicit calculations of the short-range electrostatics. For the long-range electrostatics, the PME algorithm was used. All the analysis of the simulations was done using in-house Python scripts that took advantage of the MDAnalysis Python package.[42,43]

Results and discussion

Membrane Stability

Sample preparation is described in Methods. Raman spectroscopy and IEC (Fig. 1f and g) measurements were performed across the investigated compositions and hydration levels (λ), to verify that all samples remained structurally and chemically consistent under the conditions employed for the subsequent neutron experiments (Text S1 and S2). The lack of change in the relative ratios between the 1612 cm^{-1} band and the trimethylammonium band at 755 cm^{-1} indicates no degradation of the quaternary ammonium groups on handling the RG_AEM in the OH^- form. Complementary TGA study supports the membrane stability (Fig. S1).

Identification of mobile species

Multi-resolution QENS data were acquired on 4 different spectrometers (Text S4). EFWS and IFWS (Text S5) performed at a chosen energy transfer is a fast measurement modality suited to follow the dynamics in the sample as a function of temperature. Changes in the slope of EFWS/IFWS intensity profiles as a function of temperature mark the onset of distinct dynamical processes, as previously presented.[44] The sequential activation of molecular motions in HDPE-membranes was tracked over the 2–300 K temperature range and, through Debye–Waller analysis of the signal, the mean-square atomic displacements (m.s.d.) was extracted. Fig. 2 presents representative EFWS and m.s.d. data for the OH^- form at low hydration (λ = 4, in H_2O), along with equivalent measurements for highly hydrated membranes (λ = 13) in both OH^- and Cl^- forms. As temperature varies, dynamic modes may shift in and out of the instrumental observation window: slower motions appear as elastic scattering within the energy resolution (E_{res}), while faster ones contribute to a featureless quasi-elastic background. These combined datasets therefore delineate multiple timescale regimes corresponding to temperature ranges dominated by particular scattering contributions within the combined QENS datasets.

Below 220 K (grey shaded area), the scattering profile obtained on the IRIS and SHARP spectrometers, which probe timescales shorter than 300 ps (Fig. 2a–d), is characterised by a regular loss in elastic intensity accompanied by an m.s.d. increase up to ~200 K, with an average slope $d\langle u^2\rangle/dT = 5.0 \pm 1.1 \times 10^{-4}$ Å^2 K^{-1}. The reduction in intensity is associated with an increase in proton mobility, and in this specific case, to the rotation of $-CH_3$ present in the polymer chains, well known to activate at around 100 K.[45] Upon increasing the temperature ($200 \leq T \leq 300$ K) we observe a rapid change in slope, associated with a significant increase in m.s.d.

The shape and slope of this elastic intensity drop depend on both the hydration level (Fig. 2a) and the nature of the anion (Fig. 2b), showing more mobility at λ = 13 than λ = 4, as expected (m.s.d. 0.54 against 0.43 Å^2 at 287 K). Regarding anion sensitivity, there is a significant temperature shift (~25 K) in the Cl^- form, as well as a less pronounced loss of elastic intensity at 300 K, indicating a reduced proton mobility with respect to OH^- form, at this timescale (m.s.d. is 0.85 against 0.54 Å^2 at 287 K). High-resolution data taken on IN16B provide additional insights. Assignment of the various regions in the E/IFWS to different processes (regions 1 to 4 in Fig. 2e) is performed thanks to the extra sensitivity to slow motions with respect to IRIS/SHARP. The rapid change in slope observed while increasing the temperature in the region $200 \leq T \leq 300$ K is now more pronounced, showing the detection of additional dynamics (at 300 K, m.s.d. values are enhanced up to 1.8 Å^2, Fig. 2f). The corresponding inelastic intensity data (Fig. 2g) reaches an energy-dependent maximum at ~250–260 K as the probed dynamics enter the backscattering window at ~200 K and then vanish at higher T as the motional

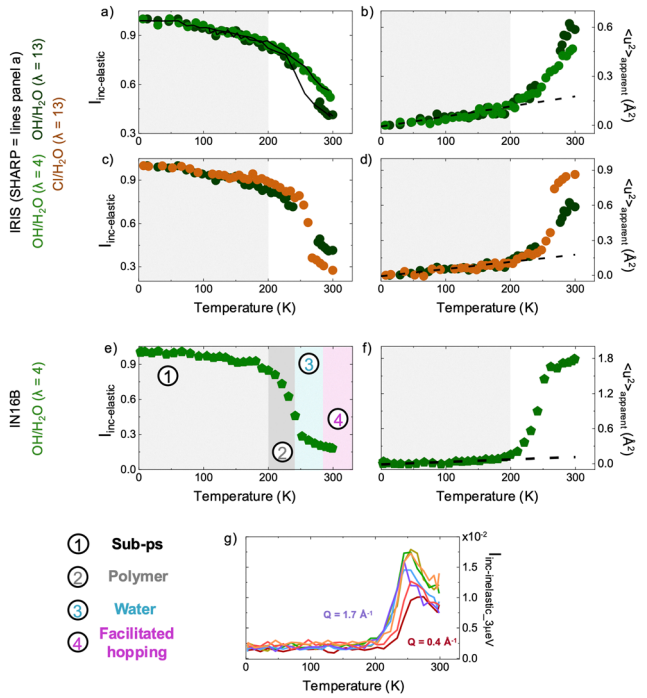

Fig. 2 (a)–(f) Q-averaged EFWS and apparent mean square displacement ($\langle u^2 \rangle_{apparent}$ – left and right panels; respectively) profiles were recorded for HDPE-TMA RG_AEM (IEC = 2.3 mmol g^{-1}) for OH^- and Cl^- form (green and brown curves; respectively). The m.s.d. slope extrapolated from data at low-T is shown as a black line. Data are recorded at $\lambda = 4$ (panels a–b) and 13 (panels a–d) using E_{res} = 17.5 and 70.0 μeV (IRIS and SHARP neutron spectrometer; respectively). High-resolution data (IN16B; E_{res} = 0.75 μeV) are presented in panel e–f for OH^- form at $\lambda = 4$. The plots are used to highlight four dynamic ranges of interest: (1) $-CH_3$ polymer dynamics (light grey); (2) side-chain polymer dynamics (dark grey); (3) water dynamics (cyan) and (4) facilitated ion hopping (purple). (g) IFWS for OH^- form at $\lambda = 4$ and at $0.4 \leq Q \leq 1.7$ $Å^{-1}$ (IN16B). Data were collected following the evolution of the inelastic intensity at a defined energy transfer (ΔE = 3 μeV; see Fig. S4).

timescales become faster than the observational window. The signal (*i.e.*, relaxation time, τ) is correlation length (Q) independent (Text S5), indicating a spatially localised process, attributed to polymer chain dynamics. Above 250 K (region 3 in Fig. 2e), the elastic intensity rapidly drops, an effect already visible in the low-resolution data. This is assigned to the onset of roto-translational water dynamics activated within hydrated AEM samples. A further moderate, but regular, decrease in intensity above $T \sim 270$ K is also recognised. The latter is very pronounced for the $\lambda = 4$ OH^-/H_2O sample, suggesting the activation of a further dynamic process occurring on a much slower timescale. The corresponding IFWS signal is found to be Q-invariant (Fig. S4), indicating localised dynamics (Fig. 2g and Fig. S4 and Text S5).

This additional process is assigned to ion hopping dynamics facilitated by water molecules bridging two OH^- groups (region 4 in Fig. 2e), similarly to what was observed in other anionic membranes.[44] It is only clearly detectable using high-resolution spectrometers, where polymer motions and roto-translational water dynamics remain active but become too fast to be observed. It is noted that a related localised hopping process also occurs when the OH^- counter-ions are replaced by Cl^-.

Ion-specific hopping mechanism

To gain a more quantitative understanding of the dynamical processes taking place in each of the temperature regions and by the different species, we analyse the multi-resolution QENS spectra. QENS broadening develops around the base of the elastic line due to scattering from relaxational or diffusional motions and must therefore be analysed using physics-informed models that describe atomic displacements. To verify the number and nature of the relaxation modes, and to assess the effects of exchanging OH^- for Cl^-, the raw QENS data for the three hydration states were compared (Fig. 3).

In the nominally "dry state", where only two water molecules remain trapped within the polymer matrix, the Cl^- form membrane shows no discernible solvent dynamics: the spectra for Cl^-/H_2O and Cl^-/D_2O are identical (Fig. 3a and b), indicating that the signal arises solely from polymer motions. In contrast, the OH^- form membrane exhibits a ~20% reduction in elastic intensity relative to the Cl^- sample (Fig. 3c), together with an additional quasi-elastic contribution (Fig. 3d). These observations reveal the presence of slow proton dynamics on the order of several hundred picoseconds, even at very low hydration levels. In fully hydrated membranes (Fig. 3e–h), the transition from Cl^- to OH^- form results in a 15–20% decrease in elastic intensity, confirming enhanced mobility in the OH^- sample and demonstrating that the nature of the counter-ion strongly influences proton mobility at the molecular level, even under swollen conditions. The magnitude of this loss varies across spectrometers (15 *vs.* 20% on SHARP – timescale: ~0.5–20 ps – and IRIS – timescale: ~5–100 ps; respectively), suggesting that multiple relaxation mechanisms with distinct timescales are affected by anion substitution.

Further insight is obtained from the intermediate hydration condition ($\lambda = 4$; Fig. 3i–p). Comparison of the OH^- and Cl^- forms in H_2O reveals a distinct difference in elastic intensity, becoming substantially more pronounced at longer timescales (~50% *vs.* ~20% for $\tau > 100$ ps and $\tau < 100$ ps, respectively). As shown in the magnified quasi-elastic wings (Fig. 3j and l), the OH^- form spectra are both more intense and broader, indicating faster proton dynamics. This demonstrates that, under identical hydration, the $OH^-/H_2O_{\lambda=4}$ sample contains more mobile protons that move more rapidly than in the Cl^- form, with particularly strong effects at long timescales, where facilitated proton hopping dominates.

Overall, these results indicate that proton dynamics are markedly enhanced in the OH^- form membrane. Isotopic substitution leads to a ~60% decrease in elastic intensity from D_2O to H_2O (Fig. 3o), confirming that the observed quasi-elastic broadening (Fig. 3p) arises from proton-bearing species (OH^- and/or H_2O). Therefore, the enhanced motions likely originate from both ions and directly coordinated water molecules (slow protons at long timescales, Fig. 3i and j), as well as from outer-shell water species (faster protons, Fig. 3k and l). Notably, the Cl^- form membrane begins to exhibit solvent dynamics at $\lambda = 4$, evidenced by the increased quasi-elastic intensity and line broadening relative to the $Cl^-/H_2O_{\lambda=2}$ sample (Fig. 3m and n), particularly when comparing H_2O and D_2O samples.

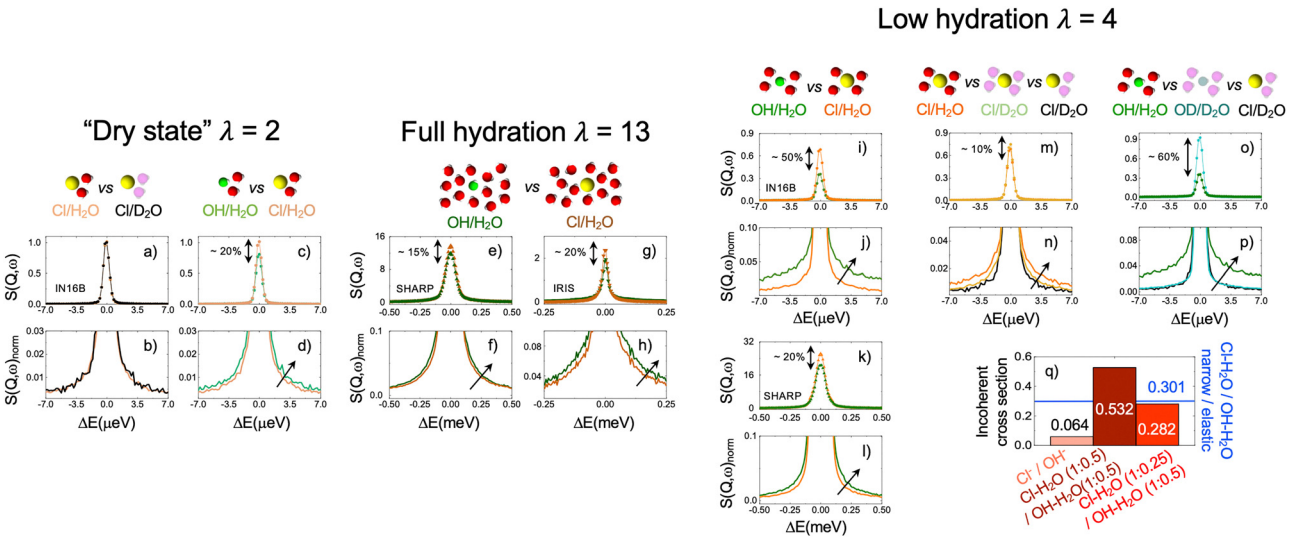

Fig. 3 (a)–(p) QENS profiles, summed over all Q-values, for RG_AEM membranes hydrated with H_2O or D_2O. Scattering data were collected at λ = 2, 4, and 13, 300 K, and using E_{res} = 70.0, 17.5, and 0.75 μeV (SHARP, IRIS, and IN16B instruments, respectively). The profiles are presented to emphasise differences in the elastic line (top panels) and normalised to unity to highlight the variation in spectral broadening (bottom panels). (q) Comparison between theoretical and experimental Cl^-/OH^- ratios. The theoretical ratio is calculated based on the incoherent scattering cross-section, while the experimental ratio is obtained from the integrated intensity ratio of the narrow quasi-elastic to elastic components. These results account for differing extents of water-mediated ion bridging (0, 0.25, or 0.5 water molecules per ion).

Beyond revealing multiple types of proton motions that depend on both hydration level and ion identity, the data also demonstrate that the nature of the counter-ion modulates the surrounding water dynamics. If the underlying mechanisms were identical, the signal intensities would be expected to scale with the incoherent neutron cross sections of the constituent atoms. However, comparison of the OH^-/H_2O and Cl^-/H_2O systems (Fig. 3i and j) shows a markedly different behaviour. The only compositional difference between the two systems is the additional proton from hydroxide, which alone cannot account for the observed ~50% decrease in total elastic intensity.

To further quantify this effect, we estimated the ratio of quasi-elastic to elastic intensity ($R_{\text{Int narrow/Int elastic}}$) by fitting the spectra with a single narrow Lorentzian in addition to the elastic contribution (Text S6 and Fig. S5). The resulting ratio between the Cl^- and OH^- samples (*e.g.*, $R = R_{Cl^-_{\text{Int narrow/Int elastic}}} \Big/ R_{OH^-_{\text{Int narrow/Int elastic}}}$) was found to be 0.301 at λ = 4. To further understand the meaning of this quantity, we calculate R using the ratio of corresponding neutron incoherent cross sections (σ in barns), under three assumptions (Fig. 3q):

(i) No water molecule participates in proton transfer.
Then, R is calculated as $\sigma_{Cl^-}/\sigma_{OH^-}$.
(ii) One water molecule every two ions mediates transfer (1 : 0.5).
Then, R is calculated as $\sigma_{Cl^-/H_2O(1:0.5)}/\sigma_{OH^-/H_2O(1:0.5)}$.
(iii) Different degrees of water mediation for each ion type (1 : 0.5 & 1 : 0.25 for OH^- and Cl^-; respectively).
Then, R is calculated as $\sigma_{Cl^-/H_2O(1:0.5)}/\sigma_{OH^-/H_2O(1:0.5)}$.

The corresponding cross-section ratios were 0.064, 0.532, and 0.282, respectively. Therefore, the third scenario best reproduces the experimental data, indicating that OH^- transport is largely water-mediated, with roughly one water molecule facilitating the interaction of every two OH^- ions. In contrast, in the Cl^- form, each water molecule mediates the coordination of approximately four Cl^- ions.

This analysis suggests that, under equivalent low-hydration conditions, the water network in the OH^- form membrane is more disrupted and dynamically active, with a larger number of water molecules participating in proton motion. This structural flexibility aligns with the macroscopic conductivity measurements, which reveal a ~20-fold enhancement in proton transport efficiency for the OH^- form compared with the Cl^- form at λ = 4 (Fig. 1b).

Fast and slow protons, static and proton-transfer mediating water

The EFWS, m.s.d., and IFWS results described above, together with the qualitative inspection of the raw QENS data as a function of the specific ion and water content, revealed multiple relaxation processes associated with the polymer matrix, ions, and water molecules. The corresponding timescales and relaxation strengths vary with the anionic form, temperature, and hydration level.

To extract quantitative parameters such as population fractions, jump distances, relaxation times, and diffusion coefficients, a fully cross-correlated analysis of multiple QENS datasets from different spectrometers was required. This involved a global fitting procedure incorporating physically meaningful models to describe the underlying dynamics. Specifically, the QENS spectra were analysed in the energy domain between 230–330 K and at hydration numbers λ = 2, 4 and 13 by fitting Lorentzian components, guided by previous studies on similar anionic/protonic systems.[44,46,47]

To best disentangle contributions, the intermediate scattering function ($I(Q,t)$; Text S7) was modelled after reconstructing the entire investigated timescale, accounting for both polymer relaxation and hydrating medium dynamics, each weighted by their relative fraction (*i.e.*, Φ_P and Φ_W – polymer and water fraction; respectively). The facilitated-hopping was further decoupled from the water dynamics by evaluating the relative populations involved in each motion (*i.e.*, $N_{W\text{-}slow}$ and $N_{W\text{-}fast}$ – slow and fast protons; respectively) as previously described:[44,48]

$$I(Q,t) = \mathrm{Amp}[\Phi_P I_P(Q,t) + \Phi_W(N_{slow} I_{w\text{-}slow}(Q,t) + N_{fast} I_{w\text{-}fast}(Q,t))]R(t) \quad (3)$$

where $R(t)$ is the normalised inverse Laplace–Fourier transform of the resolution function, and Amp is an arbitrary amplitude function. I_p and I_w represent the intermediate scattering function associated with polymer and water dynamics, respectively, and were modelled as exponential functions. Because water dynamics in the investigated system are complex, $I_{w\text{-}fast}$ (Q,t) captures both localised and long-range motions. These reflect confined dynamics at low hydration levels and Fickian diffusion emerging at high hydration, consistent with observations in other OH^- and H^+ conducting membranes.[44,48] Details of the analysis and all fitted data are provided in the SI (Fig. S6–S9).

A schematic illustration of the various motions and their corresponding parameters is shown in Fig. 4a, along with representative QENS data and the individual components used to reproduce the dynamical structure factor $S(Q,\omega)$ (Fig. 4b). Fig. 4c summarises the evolution of the dynamic parameters as a function of hydration for the OH^- and Cl^- forms.

Polymer relaxations. We first describe the fast (~2–10 ps), Q-independent polymer backbone and side-chain dynamics observed in samples lacking mobile protons within the ionic phase. These dynamics were evaluated using D_2O-hydrated samples measured across the full set of spectrometers employed in this study and were subsequently fixed as constraints in the following analyses. Localised motions emerge above 230 K, with an activation energy ($E_{a\text{-}polymer}$) of approximately 10 kJ mol^{-1} and show a decrease in relaxation time ($\tau_{polymer\_fast}$; Fig. 4c, top panel, filled black star, and Fig. S10a). This process is consistent with the γ-relaxation previously reported in dielectric measurements of HDPE.[49] The fast polymer dynamics appear to be coupled to a slower relaxation process ($\tau_{polymer\_mid}$) with a lower activation energy (~4 kJ mol^{-1}), which becomes discernible only at intermediate energy resolutions ($17.5 \leq E_{res} \leq 58.7$ μeV; Fig. 4c, top panel, filled grey star, and Fig. S10b).

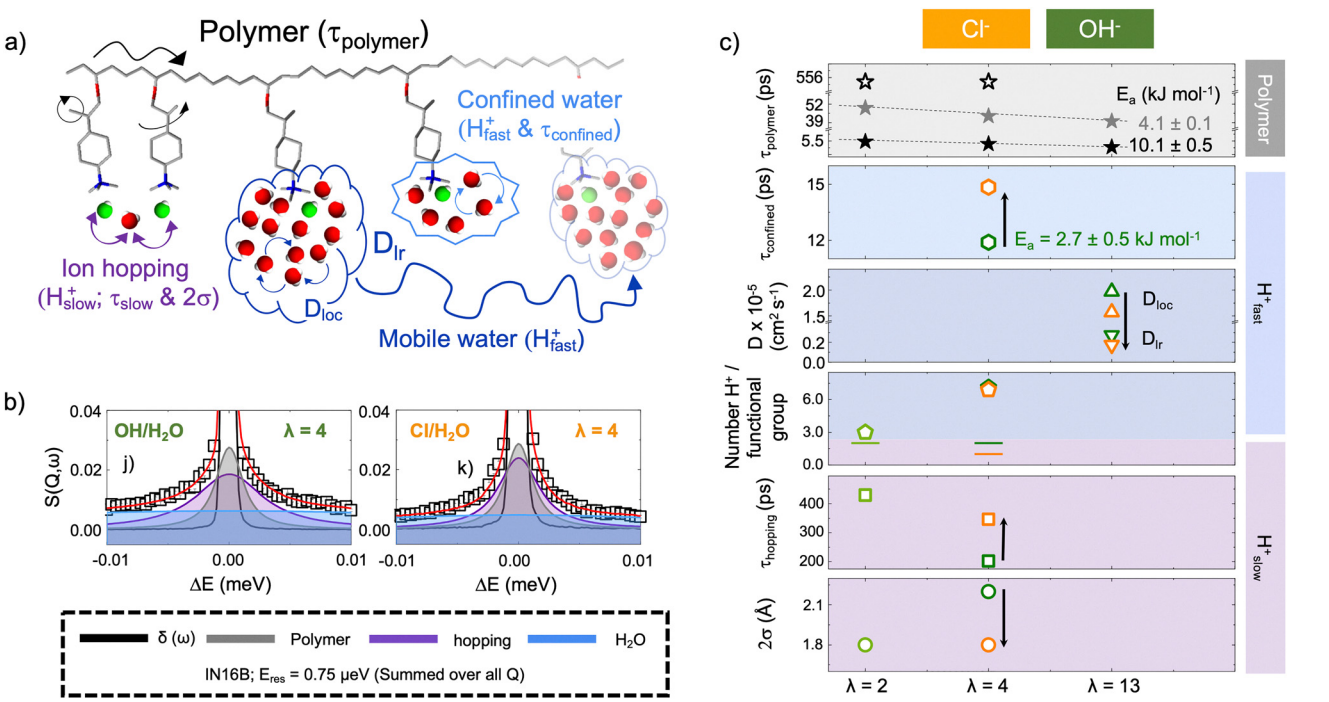

Fig. 4 (a) Schematic illustration of the distinct dynamical components contributing to the QENS signal. Polymer segmental motions ($\tau_{polymer}$: polymer relaxation time) coexist with ion-hopping dynamics (H^+_{slow}, τ_{slow}, & 2σ: number of slow protons, relaxation time associated with ion hopping, and hopping distance, respectively) and water dynamics comprising confined (H^+_{fast} & $\tau_{confined}$: number of fast protons and confined water lifetime, respectively) and mobile components, characterised by local (D_{loc}) and long-range (D_{lr}) diffusion coefficients. (b) Representative $S(Q,\omega)$ spectra for OH^- and Cl^- exchanged membranes at a hydration level of λ = 4, measured on the IN16B spectrometer (E_{res} = 0.75 μeV). Experimental data (black symbols) are fitted using contributions from polymer (grey), water (blue), and ion-hopping (purple) components. The resolution function is shown as a black line, and the overall fit is shown in red. (c) Evolution of dynamic parameters as a function of hydration level and ion form (Cl^-, OH^-). Panels display the polymer relaxation time ($\tau_{polymer}$) and corresponding activation energies (E_a), confined water lifetime ($\tau_{confined}$), local (D_{loc}) and long-range (D_{lr}) diffusion coefficients, number of H^+ per functional group, ion-hopping relaxation time ($\tau_{hopping}$), and hopping distance (2σ). OH^- form membranes exhibit enhanced water mobility and stronger coupling between polymer and water dynamics compared with Cl^- form.

Both the fast and intermediate polymer relaxations are accompanied by an additional, extremely slow component (~560 ps; Fig. 4c, open star; Fig. S10e), as evidenced by the subtle line broadening observed on the high-resolution spectrometer for the Cl^-/D_2O ($\lambda = 2$; Fig. S9b,i) and the OD^-/D_2O ($\lambda = 4$; Fig. S9e and l) contrasts. In these ionic/isotopic configurations, no ion-related dynamics are expected, since Cl^- and OD^- contribute negligibly to the incoherent neutron signal owing to their small cross sections (5.3 *vs.* 2.05 barns for Cl^- and OD^-; respectively). Likewise, water dynamics are not expected to contribute under the low-hydration D_2O conditions. The additional slow component (orange-shaded region in Fig. S9) can thus be attributed exclusively to polymer motion, as the polymer backbone remains hydrogenated. It is worth noting that, to capture these dynamic contributions accurately, the analysis was first performed considering only one narrow and one broad component. The model was subsequently refined to include three distinct dynamic processes (Fig. S9): (i) slow polymer motion (grey-shaded area), (ii) facilitated ion hopping (mauve-shaded area), and (iii) fast polymer motion coupled with localised water dynamics (light-blue-shaded area).

Number of fast and slow protons. All datasets were consistently fitted using eqn (3), allowing a clear distinction between slow protons involved in localised hopping and fast protons associated with water diffusion in confined or bulk-like environments. A clear difference is evident between the two ionic forms. At $\lambda = 4$, the number of slow protons decreases from two in the OH^- form to one in the Cl^- form. This value remains constant for the OH^- form across the investigated hydration levels ($\lambda = 2$ and 4), consistent with the presence of a stronger hydrogen-bond network and the enhanced proton mobility characteristic of hydroxide-based systems.

Water dynamics. Above $\lambda = 4$, features associated with water dynamics in the H_2O-hydrated samples emerge in the scattering profiles. The analysis reveals a Q-independent behaviour consistent with localised motions ($\tau_{confined}$ ~12 ps and E_a ~3 kJ mol^{-1} for the OH^- form; Fig. 4c, light blue panel). Comparison of the relaxation times shows that confined water in the Cl^- form relaxes more slowly than in the OH^-/H_2O system (~15 *vs.* 12 ps; Fig. 4c and Fig. S10e). By $\lambda = 13$, the water dynamics become Q-dependent, indicative of translationally mobile H_2O (Fig. S12).

At temperatures above 300 K, the OH^-/H_2O system exhibits a regular increase in diffusivity of approximately 30%, observed for both localised and long-range diffusion coefficients (D_{loc} and D_{lr}). Interestingly, at 280 K, despite a similar ~30% increase in D_{lr}, the localised dynamics remain essentially unchanged and comparable to those of bulk water (Fig. S12).

Facilitated hopping. Differences between the two ionic forms were qualitatively observed under several conditions and dynamic regimes (Fig. 3) and were subsequently confirmed by the global fitting analysis. To further substantiate these observations, the incoherent cross section and the peak integral (narrow over elastic component) were evaluated for both ionic forms (Fig. 3q). The resulting ratio reveals that distinct species contribute to the dynamics: in the OH^- form, hopping is facilitated by one water molecule bridging two ions, whereas in the Cl^- form, one water molecule appears to bridge four ions. This interpretation is consistent with the qualitative analysis and aligns with behaviour previously observed in commercial samples (Fig. S13[44]).

Importantly, a pronounced difference in the elastic line between the two ionic forms, detected even at comparable dry mass and water uptake, cannot be solely attributed to dehydration-induced crystallinity changes observed by Raman spectroscopy (Fig. 1d). The discrepancy persists across all hydration levels and instrumental resolutions (Fig. 3), and is particularly evident at $\lambda = 4$ under high-resolution conditions, where the OH^-/H_2O intensity is nearly halved (Fig. 3i). Together, these findings reinforce the notion that the two counter-ions engage in distinct hydration structures and local environments, directly influencing their respective dynamic signatures. Notably, in the Cl^- form, slow localised dynamics (*i.e.*, hopping) become apparent only above $\lambda = 4$ (Fig. 4 and Fig. S9), whereas in the OH^- form, such facilitated hopping is already detected at the lowest hydration level ($\lambda = 2$; Fig. S9). The number of dynamically coupled water molecules also differs between the two systems, approximately one water molecule per two ions in the OH^- form and one per four ions in the Cl^- form, as corroborated by the ratios (*i.e.*, $(N_{w\_fast})/(N_{w\_slow})$) obtained from fitting.

This mechanistic divergence leads to enhanced facilitated hopping in the OH^- form, which appears nearly halved in the Cl^- form ($\tau_{hopping}$ ~200 *vs.* ~350 ps for OH^- and Cl^-; respectively – Fig. 4c and Fig. S10e). The latter is accompanied by a shorter hopping distance ($2\sigma = 2.2$ *vs.* 1.8 Å for OH^- and Cl^-, respectively; Fig. 4c) and a smaller slow-population fraction (2 *vs.* 1 for OH^- and Cl^-; respectively – Fig. 4c). Interestingly, the hopping distance in the Cl^- form at $\lambda = 4$ (1.8 Å) matches that of the OH^- form at $\lambda = 2$, suggesting a more rigid, less hydrated structure in the Cl^- form, resembling the ''formally dry'' state. These distinctions are also evident in the time domain (Fig. S14), where the Cl^-/H_2O profile exhibits a more pronounced reduction in intensity, particularly at short times, compared with OH^-/H_2O. It is worth noting, however, that the kink around 10 ps may be an artefact, as the $I(Q,t)$ for Cl^-/H_2O was reconstructed from only two instrumental resolutions (broad and high) rather than three, as used for OH^-/H_2O.

At higher hydration ($\lambda = 13$), both ionic forms display an apparent slowing of localised dynamics relative to bulk water, though with distinct activation energies (~14 *vs.* ~8 kJ mol^{-1} for OH^- and Cl^-; respectively – Fig. S12). This difference in slope essentially vanishes for the long-range dynamics (~7 kJ mol^{-1}; Fig. S12). The latter agrees with conductivity-derived values at 100% RH only for the OH^- sample (6.1 ± 0.1 *vs.* 15.5 ± 2.0 kJ mol^{-1} for OH^- and Cl^-, respectively). The higher activation energy of the Cl^- sample inferred from conductivity measurements is, however, consistent with the steeper slope observed for water dynamics in the FWS (Fig. 2c).

Collectively, these results demonstrate that the distinct dynamic fingerprints of the two ionic forms stem from fundamental differences in ion–water interactions and hydration structure. The contrasting ability of OH^- and Cl^- to participate

in hydrogen bonding directly modulates local water dynamics and hopping mechanisms, thereby explaining their divergent ionic conductivities and overall membrane performance.

Characterisation of the H-bond network and link to conduction mechanism

To further examine this hypothesis, total scattering experiments were performed using the NIMROD diffractometer at ISIS. Scattering profiles were collected for the Cl^- and OH^- forms of the membrane hydrated in either D_2O or H_2O (Fig. 5a and b and Fig. S15). The data were processed by subtracting the respective profiles in D_2O and H_2O (*i.e.*, D_2O – H_2O), to remove the membrane contribution, thereby isolating correlations involving water–water and water–membrane interactions.

This subtraction procedure worked effectively for the OH^- form, yielding a liquid water-like scattering profile (Fig. 5b, left panel), indicating that the water structure remains consistent regardless of the isotopic solvent. In contrast, for the Cl^- form the direct subtraction fails in the *Q*-range corresponding to intermolecular distancing, suggesting differences between the two isotopic systems. A residual signal around 3 $Å^{-1}$ (Fig. 5a) indicates that the D_2O-hydrated sample appears more structured. This effect does not arise from experimental artefacts, as it persisted across multiple measurements and independent sample batches. The observed intensity difference may instead reflect incomplete isotopic exchange, leaving some unexchanged D_2O molecules after contrast variation.

The distinct scattering behaviour of the two ionic forms likely originates from differences in how water organises around the ions and within the polymer matrix, leading to variations in the degree of order in both water–water and water–membrane correlations.

As discussed earlier, the presence of ions can significantly modulate the structure and dynamics of water molecules. Smaller ions with higher charge densities (*e.g.*, Li^+) strongly coordinate with surrounding water molecules, forming more ordered and rigid hydration shells and disrupting the hydrogen-bonding network within them.[1,2] Conversely, larger ions with lower charge densities (*e.g.*, Cl^-) interact more weakly, resulting in diffuse, less constrained hydration structures.[1,2] Such ion-specific effects propagate beyond the first hydration shell to reshape the extended hydrogen-bond network. Hydroxide, capable of both donating and accepting hydrogen bonds, promotes a highly labile and dynamically reorganising water structure,[50] whereas chloride stabilises a comparatively more ordered hydration environment, an effect amplified in D_2O.

In highly concentrated chloride solutions, water molecules form a percolating network in which chloride ions are directly integrated.[51] Unlike dilute systems, where water primarily forms H-bonds with itself, in concentrated solutions, chloride

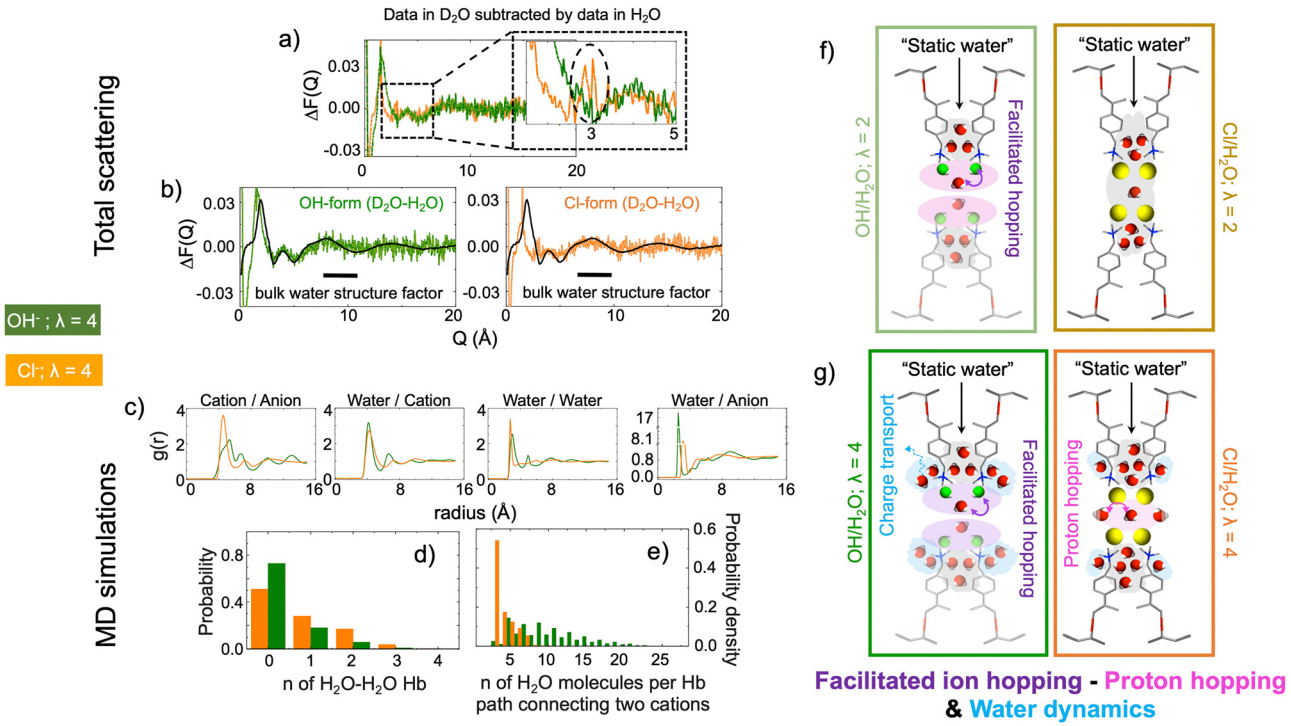

Fig. 5 (a) and (b) Comparison between scattering profiles (acquired on NIMROD, ISIS) measured at λ = 4 and 300 K. Data are presented after subtraction (*i.e.*, D_2O-profile–H_2O-profile); in the inset is highlighted the area at low-*Q* to show the extra signal at around 3 $Å^{-1}$ (panel a). Data are also presented against the water signal (black line; panel b). (c)–(e) Simulations were performed at 300 K on ionic solutions, as detailed in Table S2. The results for TMA/OH^- and TMA/Cl^- are represented by the olive and orange lines, respectively. These simulations consider various interactions, as illustrated in the plot. Panel c shows the radial distribution function, g(r); panel d reports the probability of forming hydrogen bonds (Hbs) within the water network, while panel e reports distribution of the number of water molecules within chain (formed by water molecules hydrogen bonded between two cations). (f) and (g) Schematic illustration of the facilitated hopping mechanism mediated by a molecule bridging two OH^- ions or four Cl^- ions for λ = 2, and 4 (panels f and g; respectively).

ions participate actively in the network. This leads to a mixed water–anion hydrogen-bonding structure, where the strong Cl^-/H_2O interactions distort the native water network and enhance local structuring.

At this stage, the experimental observations are further supported by Molecular Dynamics (MD) simulations performed for both ionic forms (Cl^- and OH^-) at a hydration level of $\lambda = 4$ (Table S2 and Fig. 5c–e and Fig. S16). The simulations reveal distinct mechanisms of water organisation between the two ionic forms under high salt concentration conditions. Specifically, the Cl^- form exhibits a higher average number of hydrogen bonds per water molecule (with other water molecules) compared to the OH^- form (Fig. 5e).

In the OH^- form, hydroxide ions interact with the TMA cations through a combination of hydrogen bonding and electrostatic interactions, whereas Cl^- ions engage only *via* electrostatic forces. As a result, OH^- ions draw additional water molecules into the first TMA hydration shell. Moreover, OH^- anions perturb the hydrogen bonding network by forming bridging hydrogen bonds between neighbouring water molecules, thereby displacing those that would otherwise reside in the primary hydration shell of another water molecule (Fig. 5e).

We further quantified the number of water molecules forming continuous H-bonded chains between two cations. As shown in Fig. 5e, the most probable chain length shifts from 2/3 water molecules in the Cl^- form to 4/5 in the OH^- form. This observation reinforces that OH^- disrupts both cation hydration and the overall water Hb network, consistent with trends observed in the radial distribution functions (Fig. 5c). By competing with water for cation coordination, OH^- reduces the number of direct cation–cation connectivity pathways, which facilitates charge conduction through alternative, more flexible routes. Concurrently, by forming its own hydrogen bonds with water, OH^- further distorts the network, leading to longer and less direct conduction paths. In contrast, Cl^- exerts a weaker perturbation since it does not form hydrogen bonds.

This behaviour is independent of the cation type (*e.g.*, TMA *vs.* MEPY; methylpyridinium); (Fig. S16), although a somewhat stronger OH^-/anion interaction is observed in the MEPY case. Overall, the MD simulations support the existence of a more disordered and dynamically flexible water–ion environment in the OH^- form. The resulting disruption and reorganisation of the water hydrogen-bond network facilitate proton motion within the hydration shells, enabling efficient long-range ion transfer reminiscent of "proton wires" in the water gossamer structure.[5] In contrast, the Cl^- form exhibits a more conventional hopping mechanism involving only a fraction of the available water molecules, leaving a large portion effectively immobile ("static water") and therefore unavailable to mediate fast charge diffusion across the membrane.

These conclusions are consistent with the conductivity differences observed between the two ionic forms, which exceed 80% across the entire RH-range and become particularly pronounced under low-hydration conditions (*e.g.*, ~90% difference at 65% RH, 72 *vs.* 3.5 mS cm^{-1} for OH^- and Cl^-; respectively). Although a direct comparison at high hydration levels is not straightforward, since differences in water uptake dominate the transport behaviour, the disparity observed at 65% RH ($\lambda = 4$) cannot be solely attributed to the intrinsic diffusivity differences of the two ions in infinite dilution (~60% − 5.27 *vs.* 2.03×10^{-9} m^2 s^{-1} for OH^- and Cl^-; respectively[30,31]). This substantial deviation suggests that a markedly different number of water molecules actively participate in the conduction process for each ion. In this context, the neutron scattering data, supported by molecular simulations, clearly demonstrate distinct water organisation and hydrogen-bonding environments in the two ionic forms, as schematically illustrated in Fig. 5f and g.

Conclusions

Our results reveal distinct ion-specific mechanisms governing water structuring and transport in OH- and Cl-exchanged AEMs. Building on our earlier work, demonstrating that a single water molecule is essential for facilitating OH^- transport, we now show that OH^- and Cl^- ions reorganise the hydrogen-bond network differently, thereby modulating water dynamics and ion mobility. Hydroxide ions disrupt and dynamically restructure the surrounding water environment, enabling efficient proton transfer through flexible hydrogen-bond pathways, whereas chloride ions sustain a more ordered and static hydration structure that restricts transport. While the phenomena were extensively probed on HDPE-RG_AEM membranes, this was also found on commercial samples of different chemistries (Fig. S13).

These contrasting behaviours persist across all hydration levels but become most pronounced under low-hydration conditions, where slow vehicular diffusion dominates and water diffusivity decreases markedly at elevated temperatures and over extended transport lengths. Crucially, the coexistence of "transport-active" and "structurally bound" (static) water populations, whose balance depends on both ion type and hydration, renders the local hydration number (number of water molecules per ionic group) an unreliable performance descriptor. Accounting for the fraction of static water associated with each ion offers a more accurate explanation of their distinct conductivities than classical diffusion models based on infinite dilution, particularly where Grotthuss-type structural diffusion is suppressed and charge transfer proceeds mainly *via* vehicular motion.

By bridging molecular-scale dynamics with macroscopic conductivity, these findings provide a mechanistic framework for optimising AEM-based fuel cells and related electrochemical devices. A deeper understanding of how ions interact with membrane materials, through hydration shells, hydrogen bonding, and water structuring, can inform the rational design of next-generation membranes combining high ionic conductivity, efficient water management, and long-term mechanical and chemical stability for durable, energy-efficient operation.

Author contributions

F. F. and S. L. conceived, designed, and interpreted the scattering studies. J. R. V. and A. P. P. prepared the samples, which

were characterised by J. R. V., A. P. P., and K. S., K. S., Q. B., V. G. S., M. A., J. M. Z., A. S., and T. F. H. supported and participated in the beamline experiments. C. D. L. performed all simulations. F. F. and S. L. wrote the manuscript with contributions from all authors.

Conflicts of interest

There are no conflicts to declare.

Data availability

All data supporting the conclusions of this manuscript are provided in the main text or in the supplementary information (SI) and also available from the authors upon request. Neutron data are available at: https://doi.org/10.5286/ISIS.E.RB1920607; https://doi.org/10.5286/ISIS.E.RB1920608; https://doi.org/10.5286/ISIS.E.RB2220224; https://doi.ill.fr/10.5291/ILL-DATA.9-11-1980. Supplementary information is available. See DOI: https://doi.org/10.1039/d6ee01258b.

Acknowledgements

F. F. acknowledges EPSRC for funding (EP/V057863/1). We thank the neutron scattering facilities at ILL (Grenoble, France), and ISIS (Didcot, UK) for the award of beamtime necessary to carry out these experiments. We are grateful to ISIS and ILL for neutron beamtime (https://doi.org/10.5286/ISIS.E.RB1920607; https://doi.org/10.5286/ISIS.E.RB1920608; https://doi.org/10.5286/ISIS.E.RB2220224; https://doi.ill.fr/10.5291/ILL-DATA.9-11-1980). The AEM synthesis and characterisations at the University of Surrey were funded by EP/T009233/1. TSM acknowledges funding from the EPSRC - EP/W03395X/1, EP/X023656/1.

References

1 Z. Zhang, M. Ohl, S. O. Diallo, N. H. Jalarvo, K. Hong, Y. Han, G. S. Smith and C. Do, Dynamics of Water Associated with Lithium Ions Distributed in Polyethylene Oxide, *Phys. Rev. Lett.*, 2015, **115**, 198301.
2 M. T. H. Nguyen, O. Tichacek, H. Martinez-Seara, P. E. Mason and P. Jungwirth, Resolving the Equal Number Density Puzzle: Molecular Picture from Simulations of LiCl(aq) and NaCl(aq), *J. Phys. Chem. B*, 2021, **125**(12), 3153–3162.
3 E. Mamontov, A. Faraone, E. W. Hagaman, K. S. Han and E. Fratini, A Low-Temperature Crossover in Water Dynamics in an Aqueous LiCl Solution: Diffusion Probed by Neutron Spin-Echo and Nuclear Magnetic Resonance, *J. Phys. Chem. B*, 2010, **114**, 16737–16743.
4 T. H. van der Loop, N. Ottosson, T. Vad, W. F. C. Sager, H. J. Bakker and S. Woutersen, Communication: Slow proton-charge diffusion in nanoconfined water, *J. Chem. Phys.*, 2017, **146**, 131101.
5 A. Hassanali, F. Giberti, J. Cuny, T. D. Kühne and M. Parrinello, Proton transfer through the water gossamer, *Proc. Natl. Acad. Sci. U. S. A.*, 2013, **110**(34), 13723–13728.
6 M. E. Tuckerman, K. Laasonen, M. Sprik and M. Parrinello, Ab initio molecular dynamics simulation of the solvation and transport of H_3O^+ and OH^- ions in water, *J. Phys. Chem.*, 1995, **99**(16), 5749–5752.
7 K. D. Kreuer, Proton Conductivity: Materials and Applications, *Chem. Mater.*, 1996, **8**(3), 610–641.
8 M. E. Tuckerman, D. Marx and M. Parrinello, The nature and transport mechanism of hydrated hydroxide ions in aqueous solution, *Nature*, 2002, **417**, 925–929.
9 D. Marx, A. Chandra and M. E. Tuckerman, Aqueous Basic Solutions: Hydroxide Solvation, Structural Diffusion, and Comparison to the Hydrated Proton, *Chem. Rev.*, 2010, **110**(4), 2174–2216.
10 K.-D. Kreuer, S. J. Paddison, E. Spohr and M. Schuster, Transport in proton conductors for fuel-cell applications: Simulations, elementary reactions, and phenomenology, *Chem. Rev.*, 2004, **104**(10), 4637–4678.
11 K.-D. Kreuer and A. Münchinger, Fast and Selective Ionic Transport: From Ion-Conducting Channels to Ion Exchange Membranes for Flow Batteries, *Annu. Rev. Mater. Res.*, 2021, **51**, 21–46.
12 D. A. Salvatore, C. M. Gabardo, A. Reyes, C. P. O'Brien, S. Holdcroft, P. Pintauro, B. Bahar, M. Hickner, C. Bae, D. Sinton, E. H. Sargent and C. P. Berlinguette, Designing anion exchange membranes for CO_2 electrolysers, *Nat. Energy*, 2021, **6**, 339–348.
13 R. Bance-Soualhi, M. Choolaei, S. A. Franklin, T. R. Willson, J. Lee, D. K. Whelligan, C. Crean and J. R. Varcoe, Radiation-grafted anion-exchange membranes for reverse electrodialysis: a comparison of N,N,N′,N′-tetramethylhexane-1,6-diamine crosslinking (amination stage) and divinylbenzene crosslinking (grafting stage), *J. Mater. Chem. A*, 2021, **9**, 22025.
14 J. Li, J. Qiao and K. Lian, Hydroxide ion conducting polymer electrolytes and their applications in solid supercapacitors: A review, *Energy Storage Mater.*, 2020, **24**, 6–21.
15 J. Wang, Y. Zhao, B. P. Setzler, S. Rojas-Carbonell, C. B. Yehuda, A. Amel, M. Page, L. Wang, K. Hu, L. Shi, S. Gottesfeld, B. Xu and Y. Yan, Poly(aryl piperidinium) membranes and ionomers for hydroxide exchange membrane fuel cells, *Nat. Energy*, 2019, **4**, 392–398.
16 H. Kim, S. Jeon, J. Choi, Y. S. Park, S.-J. Park, M.-S. Lee, Y. Nam, H. Park, M. Kim, C. Lee, E. E. An, J. Jung, S. Kim, J. F. Kim, H.-S. Cho, A. S. Lee and J.-H. Lee, Interfacially Assembled Anion Exchange Membranes for Water Electrolysis, *ACS Nano*, 2024, **18**(47), 32694–32704.
17 Z. Wang, G. Sun, N. H. C. Lewis, M. Mandal, A. Sharma, M. Kim, J. M. Montes de Oca, K. Wang, A. Taggart, A. B. Martinson, P. A. Kohl, A. Tokmakoff, S. N. Patel, P. F. Nealey and J. J. de Pablo, Water-mediated ion transport in an anion exchange membrane, *Nat. Commun.*, 2025, **16**, 1099.
18 C. Lu, C. Hu, Z. Chen, P. Wang, F. Feng, G. He, F. Wang, Y. Zhang, J. Z. Liu and J. Qu, Dehydration-enhanced ion-pore interactions dominate anion transport and selectivity in nanochannels, *Sci. Adv.*, 2023, **9**, eadf8412.
19 Z. Li, J. Fu, X. Zhou, S. Gui, L. Wei, H. Yang, H. Li and X. Guo, Ionic Conduction in Polymer-Based Solid Electrolytes, *Adv. Sci.*, 2023, **10**(10), 2201718.

20 D. R. Dekel, I. G. Rasin, M. Page and S. Brandon, Steady state and transient simulation of anion exchange membrane fuel cells, *J. Power Sources*, 2018, **375**, 191–204.
21 K. Yassin and D. R. Dekel, Grand challenges in anion exchange membrane energy applications, *Front. Membr. Sci. Technol.*, 2025, **4**, 1691096.
22 G. Das, J.-H. Choi, P. K. Thinh Nguyen, D.-J. Kim and Y. S. Yoon, Anion Exchange Membranes for Fuel Cell Application: A Review, *Polymers*, 2022, **14**(6), 1197.
23 L. Wang, X. Peng, W. E. Mustain and J. R. Varcoe, Radiation-grafted anion-exchange membranes: the switch from low- to high-density polyethylene leads to remarkably enhanced fuel cell performance, *Energy Environ. Sci.*, 2019, **12**, 1575–1579.
24 J. C. Douglin, J. R. Varcoe and D. R. Dekel, A high-temperature anion-exchange membrane fuel cell with a critical raw material-free cathode, *J. Power Sources Adv.*, 2020, **5**, 100023.
25 A. L. G. Biancolli, A. S. Barbosa, Y. Kodama, R. R. de Sousa Jr., A. J. C. Lanfredi, F. C. Fonseca, J. F. Q. Rey and E. I. Santiago, Unveiling the influence of radiation-induced grafting methods on the properties of polyethylene-based anion-exchange membranes for alkaline fuel cells, *J. Power Sources*, 2021, **512**, 230484.
26 L. Wang, M. Bellini, H. A. Miller and J. R. Varcoe, A high conductivity ultrathin anion-exchange membrane with 500+ h alkali stability for use in alkaline membrane fuel cells that can achieve 2 W cm^{-2} at 80 °C. J, *Mater. Chem. A*, 2018, **6**, 15404–15412.
27 T. J. Omasta, A. M. Park, J. M. LaManna, Y. Zhang, X. Peng, L. Wang, D. L. Jacobson, J. R. Varcoe, D. S. Hussey, B. S. Pivovar and W. E. Mustain, Beyond catalysis and membranes: visualizing and solving the challenge of electrode water accumulation and flooding in AEMFCs, *Energy Environ. Sci.*, 2018, **11**, 551–558.
28 V. Sproll, G. Nagy, U. Gasser, J. P. Embs, M. Obiols-Rabasa, T. J. Schmidt, L. Gubler and S. Balog, Radiation Grafted Ion-Conducting Membranes: The Influence of Variations in Base Film Nanostructure, *Macromolecules*, 2016, **49**, 4253–4264.
29 A. Zhegur-Khais, F. Kubannek, U. Krewer and D. R. Dekel, Measuring the true hydroxide conductivity of anion exchange membranes, *J. Membr. Sci.*, 2020, **612**, 118461.
30 C. A. J. Appelo, Solute transport solved with the Nernst-Planck equation for concrete pores with 'free' water and a double layer, *Cem. Concr. Res.*, 2017, **101**, 102–113.
31 P. Vanýsek, Ionic conductivity and diffusion at infinite dilution, in *Handbook of Chemistry and Physics*, CRC Press, Boca Raton, FL, 1992, 93rd edn.
32 L. Gubler, Polymer Design Strategies for Radiation-Grafted Fuel Cell Membranes, *Adv. Energy Mater.*, 2014, **4**(3), 1300827.
33 ILL beamtime: https://doi.ill.fr/10.5291/ILL-DATA.9-11-1980.
34 SIS beamtime: https://doi.org/10.5286/ISIS.E.RB1920607; https://doi.org/10.5286/ISIS.E.RB1920608; https://doi.org/10.5286/ISIS.E.RB2220224.
35 B. Frick, J. Combet and L. van Eijck, New possibilities with inelastic fixed window scans and linear motor Doppler drives on high resolution neutron backscattering spectrometers, *Nucl. Instrum. Methods Phys. Res., Sect. A*, 2012, **669**, 7–13.
36 D. T. Bowron, A. K. Soper, K. Jones, S. Ansell, S. Birch, J. Norris, L. Perrott, D. Riedel, N. J. Rhodes, A. Botti, M.-A. Ricci, F. Grazzi and M. Zoppi, NIMROD: The Near and InterMediate Range Order Diffractometer of the ISIS second target station, *Rev. Sci. Instrum.*, 2010, **81**, 033905.
37 A. K. Soper, The Radial Distribution Functions of Water as Derived from Radiation Total Scattering Experiments: Is There Anything We Can Say for Sure?, *ISRN Phys. Chem.*, 2013, 279463.
38 A. K. Soper, Inelasticity corrections for time-of-flight and fixed wavelength neutron diffraction experiments, *Mol. Phys.*, 2009, **107**, 1667–1684.
39 J. Huang and A. D. MacKerell Jr., Applications of Computational Methods to Simulations of Protein Dynamics, *J. Comput. Chem.*, 2013, **34**(25), 2134–2145.
40 S. Jo, T. Kim, V. G. Iyer and W. Im, CHARMM-GUI: A web-based graphical user interface for CHARMM, *J. Comput. Chem.*, 2008, **29**, 1859–1865.
41 J. Lee, X. Cheng, J. M. Swails, M. S. Yeom, P. K. Eastman, J. A. Lemkul, S. Wei, J. Buckner, J. C. Jeong, Y. Qi, S. Jo, V. S. Pande, D. A. Case, C. L. Brooks III, A. D. MacKerell Jr, J. B. Klauda and W. Im, CHARMM-GUI Input Generator for NAMD, GROMACS, AMBER, OpenMM, and CHARMM/OpenMM Simulations Using the CHARMM36 Additive Force Field, *J. Chem. Theory Comput.*, 2016, **12**, 405–413.
42 N. Michaud-Agrawal, E. J. Denning, T. B. Woolf and O. Beckstein, MDAnalysis: A toolkit for the analysis of molecular dynamics simulations, *J. Comput. Chem.*, 2011, **32**, 2319–2327.
43 R. J. Gowers, M. Linke, J. Barnoud, T. J. E. Reddy, M. N. Melo, S. L. Seyler, D. L. Dotson, J. Domanski, S. Buchoux, I. M. Kenney and O. Beckstein, MDAnalysis: A Python package for the rapid analysis of molecular dynamics simulations, in *Proceedings of the 15th Python in Science Confreference*, ed. S. Benthall and S. Rostrup, Austin, TX, 2016, pp. 98–105.
44 F. Foglia, Q. Berrod, A. J. Clancy, K. Smith, G. Gebel, V. García Sakai, M. Appel, J.-M. Zanotti, M. Tyagi, N. Mahmoudi, T. S. Miller, J. R. Varcoe, A. P. Periasamy, D. J. L. Brett, P. R. Shearing, S. Lyonnard and P. F. McMillan, Disentangling water, ion and polymer dynamics in an anion exchange membrane, *Nat. Mater.*, 2022, **21**, 555–563.
45 M. Prager, A. Pawlukojc, A. Wischnewski and J. Wuttke, Inelastic neutron scattering study of methyl groups rotation in some methylxanthines, *J. Chem. Phys.*, 2007, **127**, 214509.
46 Q. Berrod, S. Lyonnard, A. Guillermo, J. Ollivier, B. Frick, A. Manseri, B. Améduri and G. Gébel, Nanostructure and Transport Properties of Proton Conducting Self-Assembled Perfluorinated Surfactants: A Bottom-Up Approach toward PFSA Fuel Cell Membranes, *Macromolecules*, 2015, **48**(17), 6166–6176.
47 Q. Berrod, S. Hanot, A. Guillermo, S. Mossa and S. Lyonnard, Water sub-diffusion in membranes for fuel cells, *Sci. Rep.*, 2017, **7**, 8326.

48 J.-C. Perrin, S. Lyonnard and F. Volino, Quasielastic neutron scattering study of water dynamics in hydrated Nafion membranes, *J. Phys. Chem. C*, 2007, **111**, 3393–3404.
49 E. Suljovrujic, M. Micic and D. Milicevic, Structural changes and dielectric relaxation behavior of uniaxially oriented high density polyethylene, *J. Eng. Fibers Fabr.*, 2013, **8**, 131–143.
50 M. E. Tuckerman, A. Chandra and D. Marx, Structure and dynamics of OH^-(aq), *Acc. Chem. Res.*, 2006, **39**, 151–158.
51 I. Pethes, I. Bako and L. Pusztai, Chloride ions as integral parts of hydrogen bonded networks in aqueous salt solutions: the appearance of solvent separated anion pairs, *Phys. Chem. Chem. Phys.*, 2020, **22**, 11038.